

Supporting Information

Polymer Infiltration into Metal-organic Frameworks in Mixed-matrix Membranes Detected In Situ by NMR

Pu Duan^{1†}, Jessica C. Moreton^{2†}, Sergio R. Tavares³, Rocio Semino³, Guillaume Maurin^{3,*}, Seth M. Cohen^{2,*}, Klaus Schmidt-Rohr^{1,*}

¹Department of Chemistry, Brandeis University, Waltham, MA 02453, USA

²Department of Chemistry and Biochemistry, University of California, La Jolla, San Diego, CA 92093, USA

³Institut Charles Gerhardt Montpellier UMR 5253 CNRS, Université de Montpellier, Place E. Bataillon, 34095 Montpellier Cedex 05, France

†These authors contributed equally to this research

Table of Contents

Computational details.....	S2
NMR details.....	S3
Experimental details.....	S5
Materials.....	S5
Synthetic procedures.....	S5
Materials characterization.....	S6
Additional experimental results.....	S8
References.....	S26

COMPUTATIONAL DETAILS

Atomistic models for poly(vinylidene fluoride) (PVDF) and poly(ethylene oxide) (PEO) were constructed following a previously reported strategy based on the use of the codes *polymatic*¹ and *lammmps*.² Bonded contributions to the force field were modeled as harmonic potentials for the stretching and bending modes and as cosine-based functions for the dihedral angles. Non-bonded interactions were treated as a summation of 12-6 Lennard-Jones (LJ) and Coulomb potentials as detailed in previous work.³ Coulombic contributions were computed by the Ewald summation, considering the Electrostatic Potential Fitting (ESP) partial charges estimated by Density Functional Theory (DFT) calculations on the monomer using the PBE (Perdew-Burke-Ernzerhof) functional⁴ combined with a Gaussian basis set. The LJ potential parameters were taken from the DREIDING force field.⁵ The crossed LJ interactions were computed by using the Lorentz–Berthelot mixing rules.⁶ The cutoff was set to 15 Å. The resulting polymer models contain 988 and 991 monomers for PVDF and PEO, respectively. They occupy similar volumes and are large enough to prevent interactions between the MOF slabs through the periodic boundary when polymer and MOF are put together in the simulation box.

The surface model of the dehydrated UiO-66 material was constructed by first optimizing the primitive cell at the DFT level, using the Quickstep module of the CP2K software.⁷ The PBE functional⁴ was used along with a combined Gaussian basis set and plane wave pseudopotential strategy as implemented in CP2K. Further details of the basis set and the treatment of the dispersion forces are described elsewhere.³ The Bravais-Friedel-Donnay-Harker (BFDH)⁸⁻¹⁰ method was applied in order to identify the most stable surfaces of this MOF, which led to the selection of the [101] surface. The surface was then reconstructed to ensure dipole neutrality and capped by OH⁻ and H⁺ groups. The LJ parameters, the ESP partial charges as well as the description of the bonded contributions to the force field of the MOF model are detailed elsewhere.³

MOF and polymer were combined to generate the interface model. Seven cycles of three molecular dynamics (MD) simulations were performed, each consisting of two simulations in the NVT and one in the NP_nT ensemble, where P_n is the pressure component in the direction perpendicular to the slab. The first simulation in each cycle was conducted at 600 K, while for the other two it was set to 300 K. Pressure was increased in the first three cycles until it reached a maximum value of 1

kbar and then decreased down to ambient pressure in the remaining four cycles, in order to pack the polymer to a reasonable density. To further explore the penetration of polymer chains into the open pores of the MOF surface, a 1 ns MD simulation was performed in the *NVT* ensemble at 2000 K. This high temperature enabled the polymer to overcome the energy barrier to penetrate the MOF pores. Thereafter, data were collected from a MD simulation in the *NPT* ensemble at $T = 300$ K and at $P = 1$ bar lasting 10 ns with a 1 fs time step.

NMR DETAILS

Model Development. SEM images of UiO-66 and UiO-66/PEO show nearly spherical 150-nm diameter MOF particles, see Figures S2-S6. On this basis, Figure 1 and Figure S10 compare two structural models of MOF/PEO MMMs with realistic dimensions and PEO volume fractions, specifically for 80 wt% UiO-66 / 20 wt% PEO. Since the densities of the MOF and of PEO are both close to 1.2 g/cm^3 , the volume fractions are nearly equal to the known mass fractions. The models differ distinctly in the PEO distribution. The model in Figure 1c (left) and Figure S10 (left) assumes a homogeneous coating of PEO on the MOF particle surface, while the others (Figure 1c, right, and Figure S10, right) assumes a homogeneous PEO distribution throughout the volume of the MOF (i.e. in the pores, which are not resolved at the scale of the schematic). It is interesting to note that a 5-nm thin layer of PEO on the surface of the 150-nm diameter particle accounts for 20% of the total volume (since $([150 + 2 \times 5]/150)^3 = 1.21$).

Effect of the MOF on PEO Dynamics. The relaxation of PEO with a short $T_{1\rho}$ of 0.8 ms reflects large-amplitude segmental motions with rates near 200,000/s, since the resulting fluctuating fields drive the spin-lattice relaxation in the rotating frame. Motions with that critical rate $k = |\omega_1| = \gamma B_1 = 2\pi \cdot 40 \text{ kHz}$ produce a minimum $T_{1\rho}$ of ~ 0.7 ms for the amorphous layers in semicrystalline PEO.¹¹ This amorphous PEO reaches the $T_{1\rho}$ value of 0.8 ms at 50 K below ambient temperature.¹¹ Thus, the data indicate a more than 10-fold slow-down of PEO, i.e. dynamic constraints imposed by the UiO-66 pore walls. Interestingly, the short relaxation time (i.e. high relaxation rate) points to large motional amplitudes of PEO in UiO-66, similar as in free

amorphous PEO, whose spin relaxation is barely faster even at the $T_{1\rho}$ minimum. At 300 K, PEO is ~ 90 K above its glass transition temperature and therefore moves so fast that its $T_{1\rho}$ relaxation is significantly slowed down;¹¹ this is confirmed by the comparison of the relaxation of free PEO vs. PEO in UiO-66 in Figure 3b.

Short $T_{1\rho}$ in MMMs. ^1H spin exchange is likely the main reason for the dramatic shortening of UiO-66-linker $T_{1\rho}$ induced by PEO: As the ^1H magnetization of PEO relaxes on the sub-millisecond scale, spin exchange (though slowed down by a factor of ~ 3 by spin lock and MAS) resupplies PEO with magnetization taken from the MOF linkers, which therefore experience faster relaxation.

PVDF Surface Adhesion Model Development. Due to the low proton density of the neat MOF, the spin diffusion coefficient is reduced relative to the value for typical rigid polymers quoted above. Assuming $D_{\text{MOF}} = 0.1 \text{ nm}^2/\text{ms}$, the thickness of the MOF layer polarized by spin diffusion from the particle surface within $t_{\text{se}} = 200 \text{ ms}$ is roughly $\Delta x_{\text{rms}} = \sqrt{2D_{\text{MOF}}t_{\text{se}}} = 6 \text{ nm}$, corresponding to a $\sim 25\%$ volume fraction of each particle, which within the uncertainties is in agreement with the experimental observation ($30 \pm 7\%$).

PVDF Cross-Peak Intensity Calculation. The intensity of the $\text{bdc}^{2-}/\text{PVDF}$ cross peaks gradually increases with spin-exchange time. The bdc^{2-} proton to PVDF cross peak is small, 0.24:1 aromatic H:CH₂ by integration, even after 200 ms of spin diffusion. After full equilibration, it increases to 1.7:1, the proton ratio of the 70:30 UiO-66/PVDF material (by comparison, the aromatic H:CH₂ proton ratio is 0.74:1 for 80:20 UiO-66/PEO, which matches the observed peak ratio in Figure 4a). Normalized cross peak intensities calculated on this basis (e.g., $0.24/1.24/(1.7/2.7) = 0.3$ after 200 ms) for this material have been included in Figure 4b.

NMR Evidence of Excess PEO. Additional PEO is observed by PXRD, NMR and DSC to form a semicrystalline structure outside the MOF. In NMR, the signal of crystalline PEO is difficult to observe due to its helical jump motions¹² that shorten $T_{1\rho}$ ¹¹ and broaden the ^{13}C resonance due to interference with ^1H decoupling. However, the sharp signal of amorphous PEO is quite easy to detect in both ^{13}C and

^1H NMR spectra (see Figures S11 and S12). The ^1H spectrum shows that there is no (<10%) free PEO in 80:20 UiO-66/PEO, consistent with the absence of a melting peak in DSC (Figure S15). As expected, the mobile PEO does not show significant cross peaks with the aromatic H in HetCor spectra, see Figure S18, since it is separated from the MOF by tens of nanometers, on average. The corresponding non-equilibrated magnetization distribution is reflected in the lack of agreement of parallel cross sections through the HetCor spectrum, see Figure S18. *Within* the MOF, the linker-PEO contact is similar as in 80:20 UiO-66/PEO; this can be demonstrated by the nearly matching ^{13}C spectra associated with the aromatic ^1H magnetization originating from the MOF linkers (see Figure S18). Only the integrated intensity of the cross peak of 50:50 (and also of 70:30) UiO-66/PEO is about 60% larger than that of 80:20 UiO-66/PEO, due to the more complete pore filling.

SYNTHESIS AND CHARACTERIZATION DETAILS

Synthetic Procedures

General. All solvents and starting materials were purchased from chemical suppliers and used without further purification (Sigma Aldrich, Arkema, Alfa Aesar, EMD, and TCI).

Large-Scale Synthesis of UiO-66. Synthesis of UiO-66 was performed via a reported procedure.¹³ Zirconium(IV) chloride (1.45 g, 6.2 mmol) and terephthalic acid (1.04 g, 6.2 mmol) were dissolved in 360 mL molecular sieve-dried DMF via sonication (<1 min). Glacial acetic acid (10.6 mL, 186 mmol) was added and the mixture was sonicated an additional 1 min to fully mix. The mixture was portioned evenly between 24 vials (20 mL, PTFE-lined caps). The vials were then placed in a preheated 120 °C oven for 24 h. After cooling to ambient temperature, the particles were collected by centrifugation (fixed-angle rotor, 5500 rpm, 10 min), followed by washing with 3×10 mL DMF and 3×10 mL MeOH. The particles were then soaked in MeOH for 3 d, with solvent changed daily, before being dried under vacuum at room temperature. Yield: 1.25 g (73%)

UiO-66/PEO MMM Fabrication. UiO-66 was synthesized according to the procedure reported above, then dispersed in acetone (3.5 wt% MOF) via sonication.

PEO ($M_z = 900,000$ g/mol, PDI = 1.2; purchased from Sigma-Aldrich) was dissolved in water to a honey-like viscosity (3.5 wt%). The two component solutions were then combined in the appropriate ratios to yield mixtures resulting in 30-80 wt% MOF-loaded MMMs, which were ultrasonicated for 1 h. The resulting solution was then concentrated by rotary evaporation, removing the acetone, and yielding a homogeneous 'ink' of MOF and polymer in water. Using a draw-down method, the MOF/PEO solution was transferred to an aluminum foil substrate and then cast with a MTI Corporation MSK-AFA-II automatic thick film coater using an adjustable doctor blade set to 1 mm, at a speed of 25 mm/second. The as-cast films were then oven-cured at 70 °C until dry (roughly 1h) and the aluminum backing was peeled away with tweezers. Most MMMs were composed of a total of 200-500mg of combined MOF and polymer components.

UiO-66/PVDF MMM Fabrication. UiO-66 was synthesized according to the procedure reported above, then dispersed in acetone (3.5 wt% MOF) via sonication. PVDF ($M_w = 750,000$ g/mol, PDI = 2.2; polymer and characterization data obtained from Arkema) was dissolved in DMF to a honey-like viscosity (7 wt%) then the MOF and polymer solutions were mixed to generate a 70:30 weight ratio of MOF to PVDF, and ultrasonicated to homogeneity. The resulting solution was then concentrated by rotary evaporation, removing the acetone, and yielding a homogeneous 'ink' of MOF and polymer in DMF. Using a draw-down method, the MOF/PVDF solution was transferred to an aluminum foil substrate and then cast with a MTI Corporation MSK-AFA-II automatic thick film coater using an adjustable doctor blade set to 500 μm , at a speed of 25 mm/second. The as-cast films were then oven-cured at 70 °C until dry (roughly 1h) and the aluminum backing was peeled away with tweezers.

Materials Characterization

Powder X-ray Diffraction (PXRD). PXRD data was collected at room temperature on a Bruker D8 Advance diffractometer running at 40 kV, 4 mA for Cu K α ($\lambda = 1.5418$ Å), with a scan speed of 0.5 sec/step, a step size of 0.02° in 2 θ , and a 2 θ range of 5-50° at room temperature. Sample holders used were zero-background Si plates (p-type, B-doped) from MTI Corp. Well-type sample holders (depth = 0.5 mm) were used for powder samples. MMM and pure-polymer samples were affixed to flat sample holders using double-sided Scotch tape.

N₂ Sorption Analysis. Approximately 50 mg of sample were placed in a tared sample tube and degassed at 70 °C on a Micromeritics ASAP 2020 Adsorption Analyzer until the outgas rate was <5 mmHg (12-48 h). Post-degas, the sample tube was weighed, and then N₂ sorption isotherm data was collected at 77 K on a Micromeritics ASAP 2020 Adsorption Analyzer using a volumetric technique. BET surface areas were then determined from analysis of the Rouquerol¹⁴ plots of the isotherm data, using 4-10 data points each. The guidelines set forth by Rouquerol¹⁴ use four criteria to obtain the most accurate BET surface area values for microporous materials such as MOFs. Further work by Snurr,¹⁵ specific to UiO-66, recommends the implementation of criteria I-III to obtain the most accurate BET area measurement for this specific material (since criteria IV is not met in UiO-66).¹⁵ Criteria I, that BET constant C must be positive, and criteria II, that the value $V(1-p/p_0)$ must increase with increasing p/p_0 for all points chosen, are both true for the UiO-66 and MMMs in this study. Similarly, criteria III states that the total monolayer loading should correspond to a relative pressure within the selected linear region and holds true for our measurements on UiO-66 and all MMMs.

Scanning Electron Microscopy (SEM). MMMs were placed on conductive carbon tape on a sample holder and coated using an Ir sputter-coating for 7 s. A FEI Quanta 250 scanning electron microscope was used for acquiring images using a 10 kV energy source under vacuum at a working distance of 10 mm.

TGA Analysis. MOF and MMM samples (5-10 mg) were weighed and placed in alumina crucibles. Samples were run under dry N₂ gas at a flow rate of 70 mL/min from 30°C – 550°C at a heating rate of 5 °C/min on a Mettler Toledo TGA/DSC 1 STARe system.

DSC Analysis. MOF and MMM samples (5-10 mg) were weighed and placed in alumina crucibles. Samples were run under dry N₂ gas at a flow rate of 70 mL/min on a Mettler Toledo TGA/DSC 1 STARe system. Samples were first heated to 80 °C at 10 °C/min to remove the thermal history, then cooled at 10 °C/min to 30 °C. The sample was then held at 30 °C for 10 min to stabilize the temperature reading, then heated to 80 °C at 5 °C/min.

ADDITIONAL EXPERIMENTAL RESULTS

Table S1. BET surface area measurements and constants are given below for all MMMs tested.

<i>Polymer</i>	<i>MOF</i>	<i>% MOF</i>	<i>BET SA (m²/g)</i>	<i>BET Constant C</i>	<i>BET Constant Q_m (mmol/g)</i>
--	UiO-66	100	1380	2417	14.16
<i>PVDF</i>	UiO-66	70	780	1523	8.00
<i>PEO</i>	UiO-66	30	< 5	--	--
		50	< 5	--	--
		70	37	199	0.38
		80	480	10658	4.94

Table S2. Theoretical and calculated (from TGA trace, Figure S25) MOF content for all PEO MMMs.

<i>Polymer</i>	<i>MOF</i>	<i>% MOF (theoretical)</i>	<i>% MOF (calculated)</i>
<i>PEO</i>	UiO-66	30	30
		50	47
		70	69
		80	79

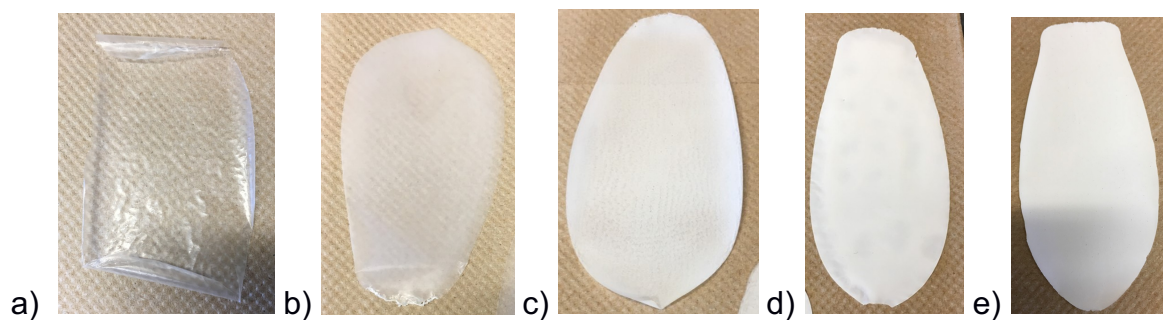


Figure S1. Full-size MMMs in PEO at a) 0 wt% UiO-66, b) 30 wt%, c) 50 wt%, d) 70 wt% and e) 80 wt% demonstrate that they are continuous, uniform and easily delaminate from the Al foil substrate. Each MMM is roughly 5 cm x 12 cm in size.

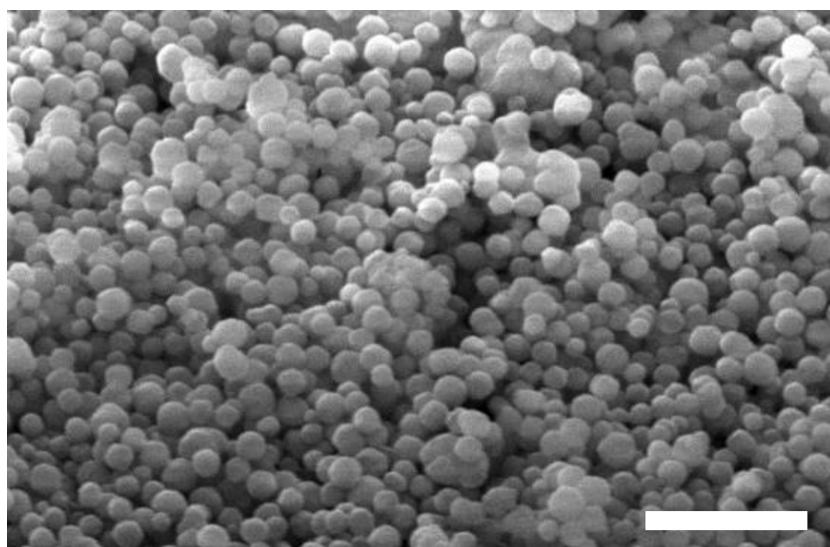


Figure S2. SEM image of as-synthesized UiO-66 (scale bar is 1 μm). This image shows the uniform ~ 150 nm diameter size and roughly spherical morphology of the particles.

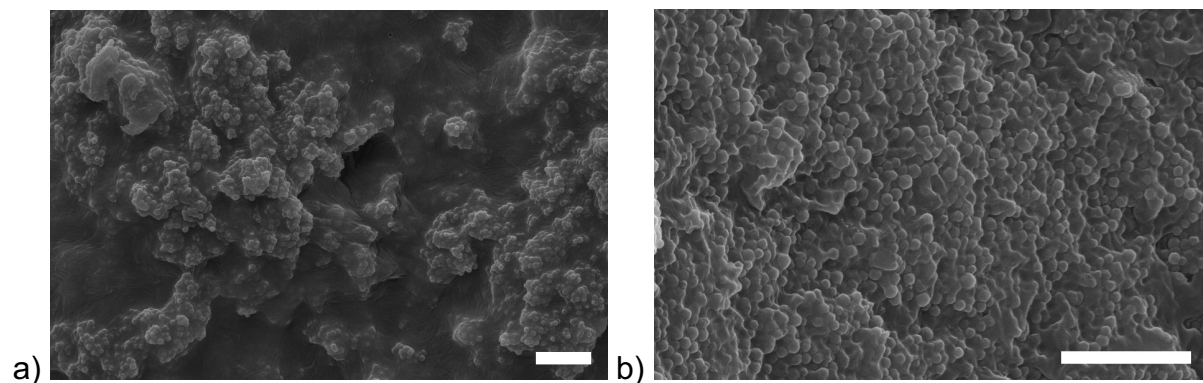


Figure S3. Images of 30 wt% UiO-66/PEO MMMs on a) the top side of the MMM and b) the MMM cross-section, with MOF visible as small round particles in a matrix of darker polymer. Scale bars are 2 μ m.

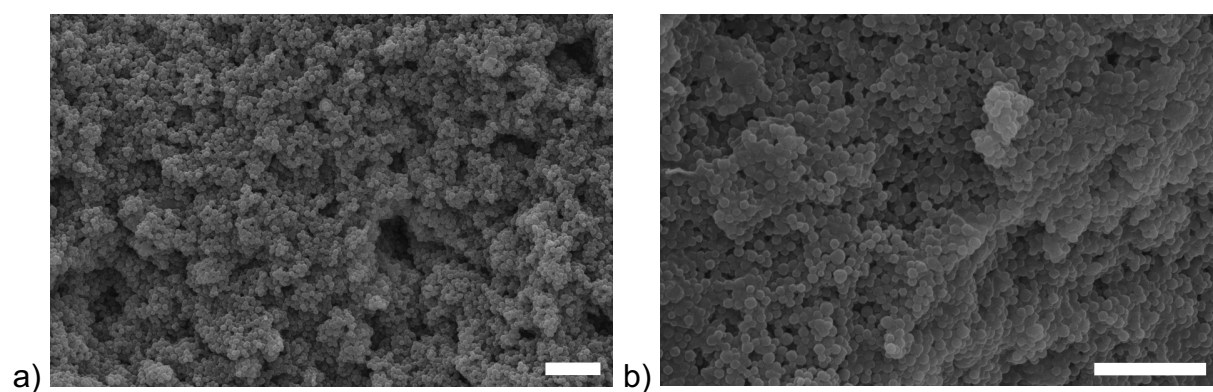


Figure S4. Images of 50 wt% UiO-66/PEO MMMs on a) the top side of the MMM and b) the MMM cross-section. Scale bars are 2 μ m. MMMs appear far more MOF-dominant, with some evidence of polymer matrix visible connecting the particles in the cross-section of the MMM.

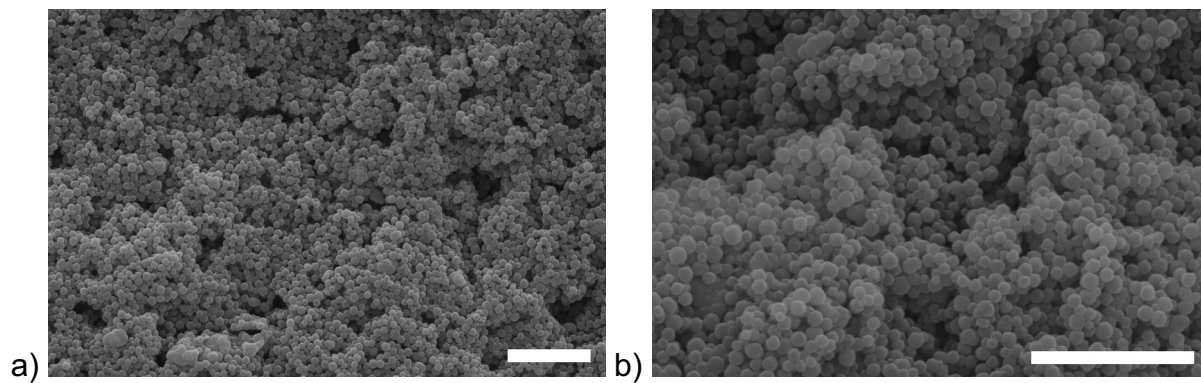


Figure S5. Images of 70 wt% UiO-66/PEO MMMs on a) the top side of the MMM and b) the MMM cross-section. Scale bars are 2 μm . The polymer matrix is no longer visible in these images, with MMMs appearing extremely MOF-dominant.

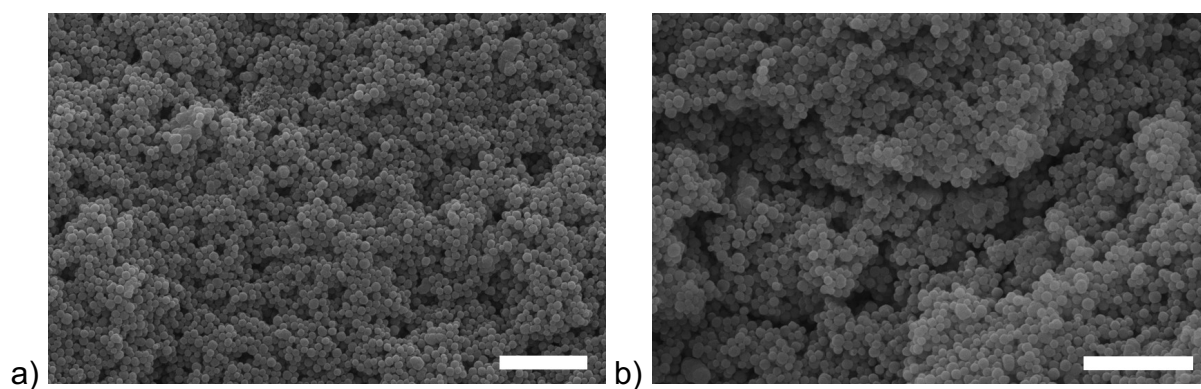


Figure S6. Images of 80 wt% UiO-66/PEO MMMs on a) the top side of the MMM and b) the MMM cross-section. Scale bars are 2 μm . The polymer matrix is no longer visible in these images, with MMMs appearing extremely MOF-dominant.

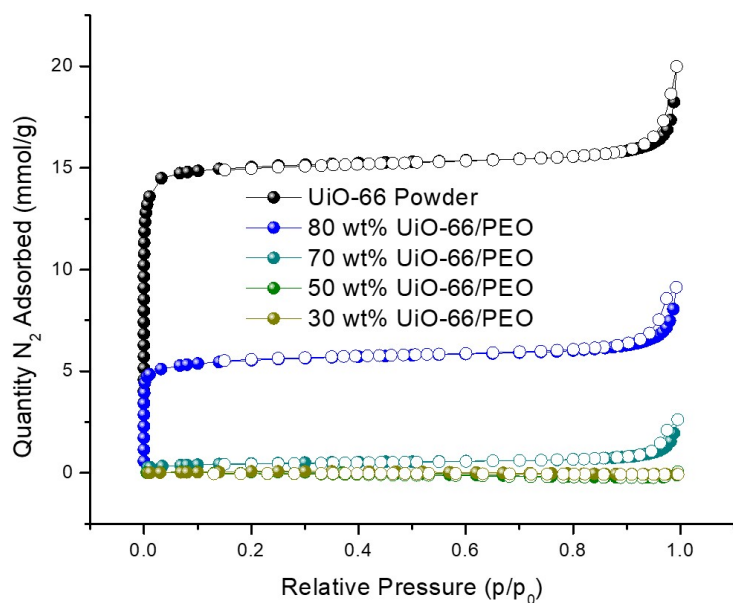


Figure S7. N₂ sorption isotherms collected at 77 K of all UiO-66/PEO MMMs compared to the starting UiO-66 powder. Little to no MOF surface area is seen below 80wt% UiO-66 in PEO, while the 80wt% UiO-66/PEO MMM demonstrates partial recovery of UiO-66 microporous character.

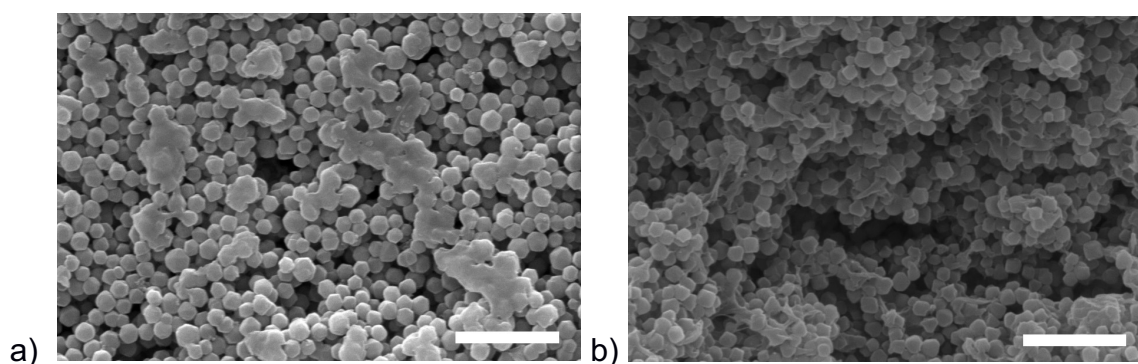


Figure S8. SEM images of 70 wt% UiO-66/PVDF MMMs on a) the top side of the MMM and b) the MMM cross-section. Scale bars are 1 μm. The continuous polymer matrix is partly visible in these images, with MMMs appearing extremely MOF-dominant.

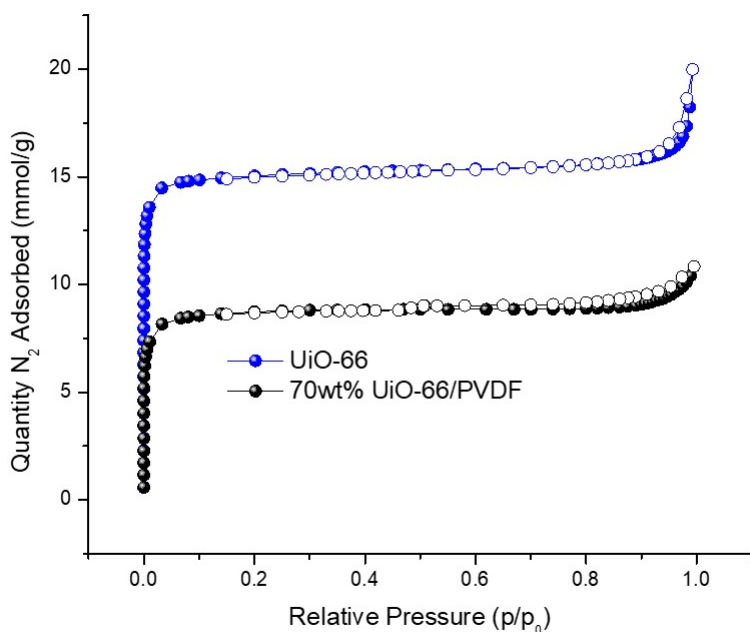


Figure S9. N₂ sorption isotherms collected at 77K of UiO-66/PVDF MMM compared to the starting UiO-66 powder. The UiO-66/PVDF MMM trace shows that access to UiO-66 micropores is retained within the PVDF matrix.

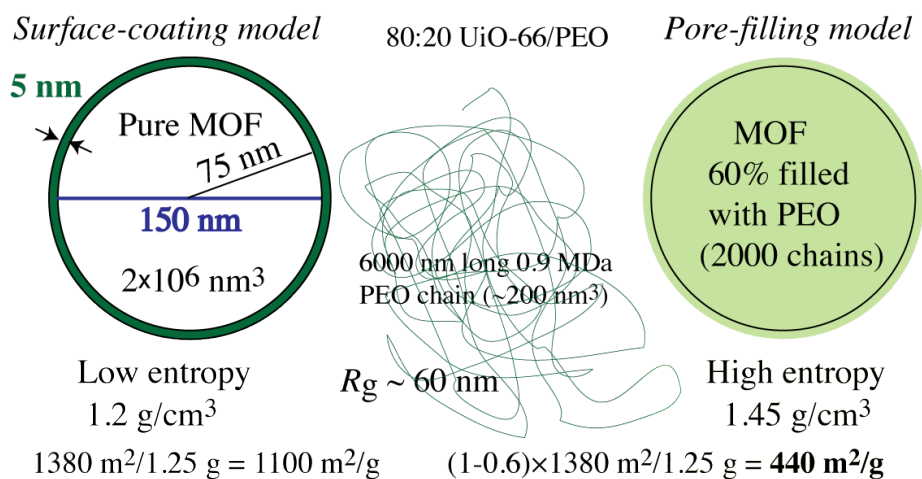


Figure S10. Two distinct models of 80:20 wt:wt UiO-66/PEO with particle size from SEM and realistic volume fractions. Left: surface-coating model; right: homogeneous pore-filling model. Center: Approximate dimensions of a typical PEO chain.

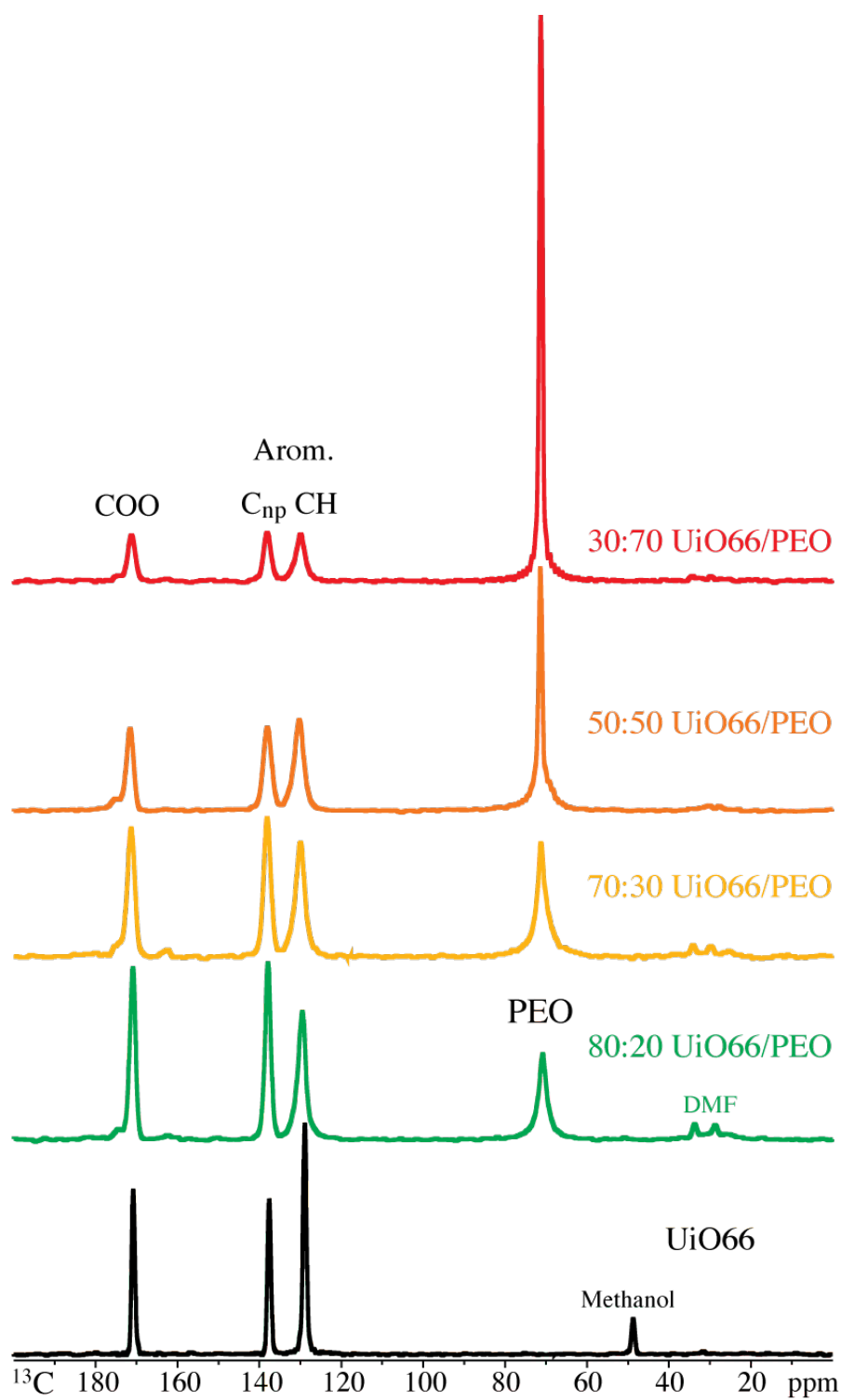


Figure S11. Full multiCP ^{13}C NMR spectra of UiO-66/PEO membranes as a function of PEO content. Spinning frequency: 14 kHz.

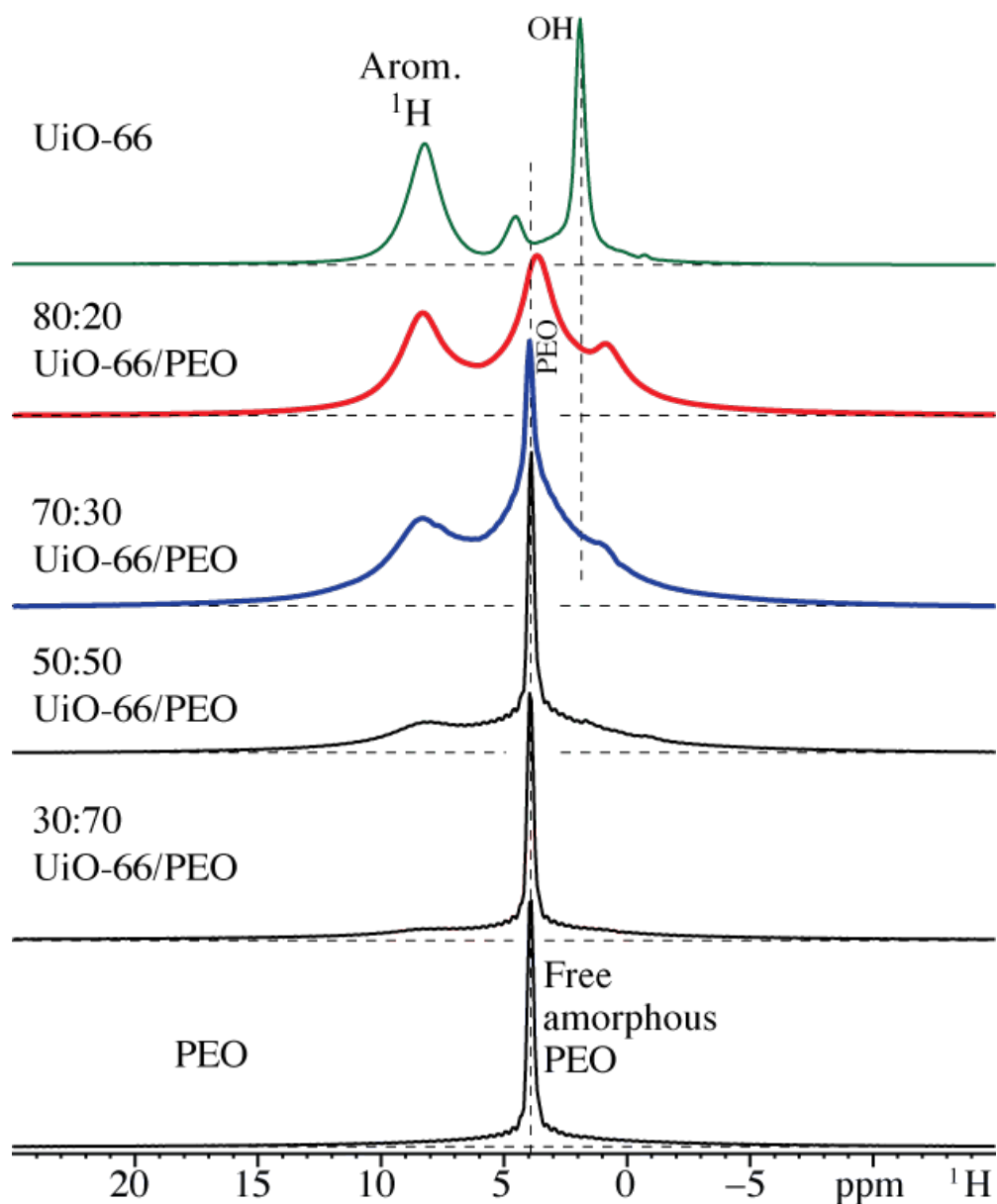


Figure S12. ^1H NMR spectra of UiO-66-PEO membranes with varying UiO-66 content as indicated, and of the pure components, recorded at 14 kHz MAS. The sharp peak at 3.9 ppm is due to highly mobile PEO in amorphous layers of the semicrystalline morphology. The widths of the aromatic-proton peaks are compared in Figure 2b. The increase in the width of the aromatic proton resonance in Figure 2b can be attributed to dipolar couplings of these protons to those of PEO, again on the sub-nanometer scale since dipolar couplings decreases strongly with distance.

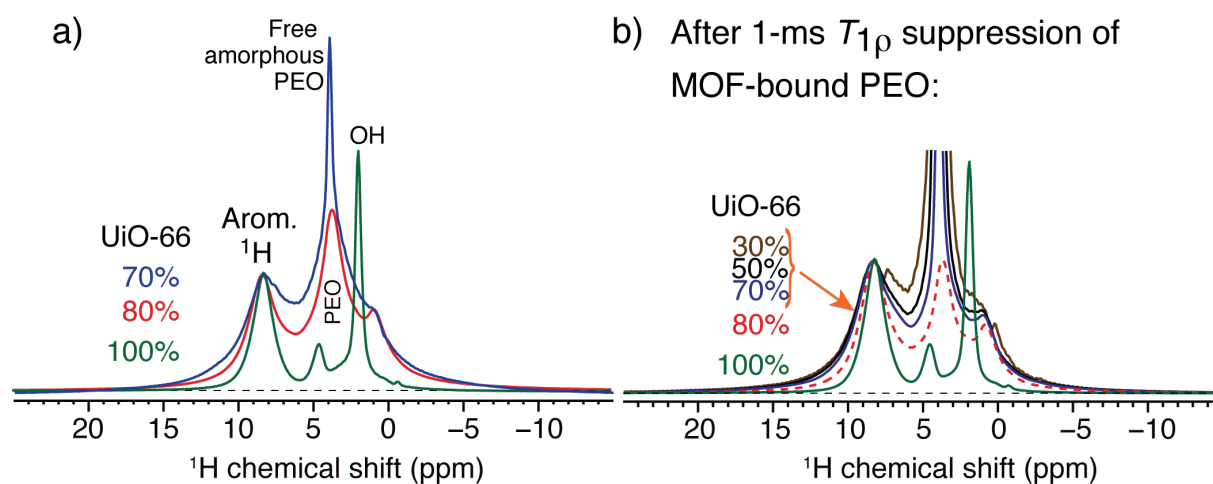


Figure S13. (a) Comparison of ^1H NMR spectra (see Figure 2b) of UiO-66/PEO MMMs with varying PEO content, and of pure UiO-66. (b) Comparison of spectra after partial suppression of the signal of MOF-bound PEO by a 1-ms $T_{1\rho}$ filter.

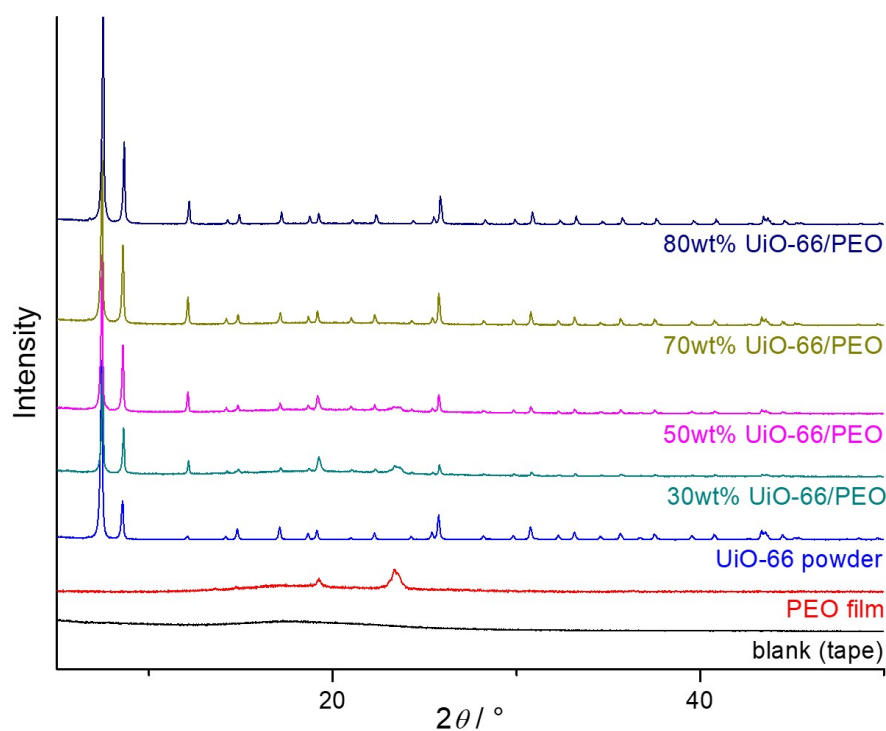


Figure S14. PXRD patterns of PEO MMMs compared to UiO-66, PEO, and a blank background. The polymer alone displays mostly amorphous character, with small features at 19° and 23° . The MMMs show the same powder pattern as UiO-66 alone, demonstrating that the MOF remains highly crystalline within the MMM.

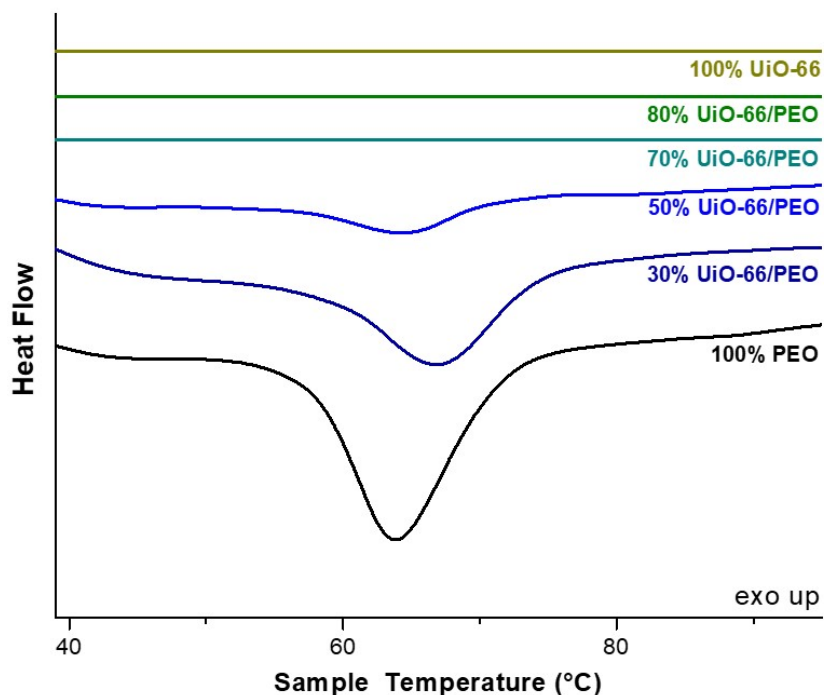


Figure S15. DSC traces of UiO-66/PEO MMMs at different MOF loadings shown above. MMMs above 50 wt% UiO-66 show no visible melt event, which may indicate significant disruption of crystalline polymer chain packing in MMMs above 50 wt% UiO-66.

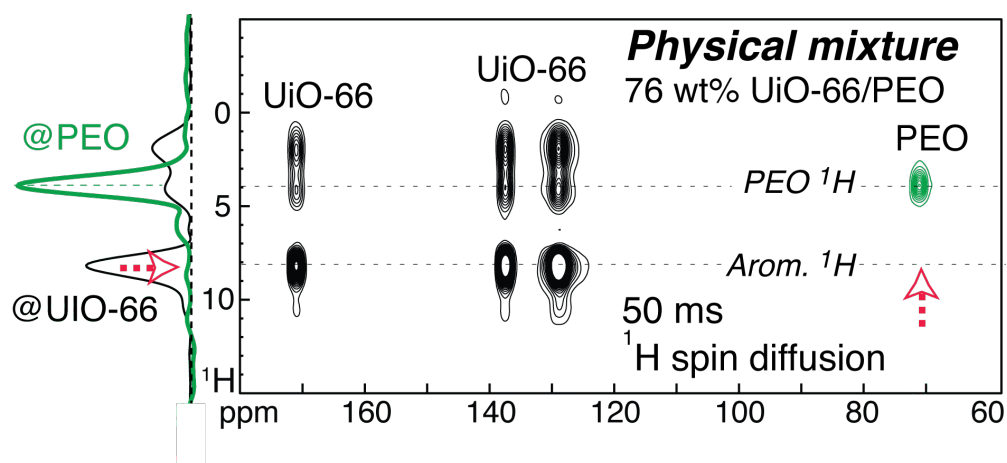


Figure S16. Extent of MOF–PEO contacts observed in ^1H - ^{13}C HetCor NMR spectrum of physical mixture of UiO-66 and PEO with ^1H spin exchange. No cross peaks indicating magnetization transfer are observed in a physical mixture.

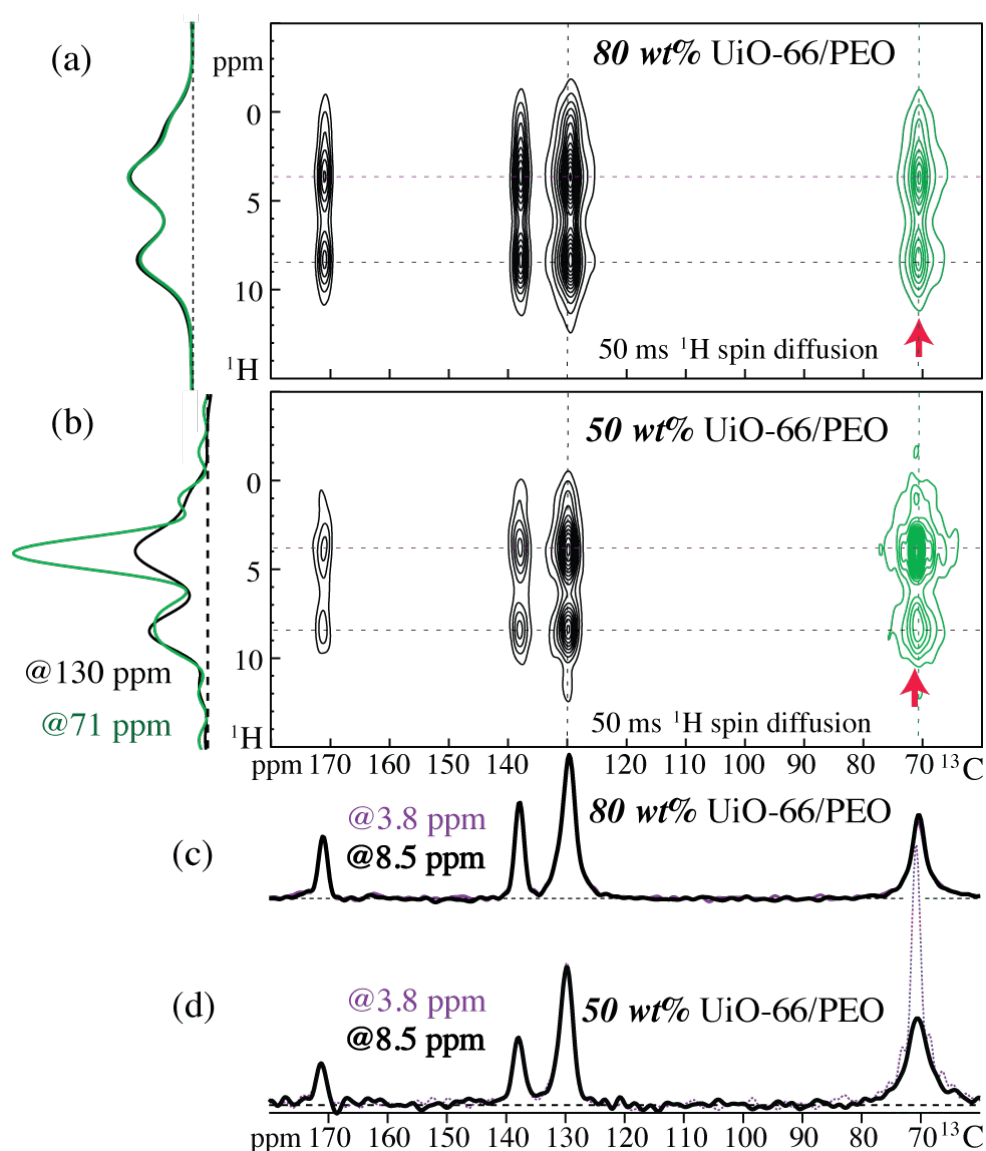


Figure S17. Extent of MOF–PEO contacts observed in the ^1H - ^{13}C HetCor NMR spectrum of 50:50 UiO-66/PEO with ^1H spin exchange in (b), compared with the spectrum of 80:20 UiO-66/PEO shown for reference in (a). (c) Horizontal cross sections of the spectrum in a) at the OCH_2 resonance (dashed purple line) and at the aromatic H resonance (solid black line), scaled vertically for best match. The cross sections are nearly indistinguishable which is the hallmark of magnetization equilibration. (d) Analogous cross sections from the spectrum in (b). The cross section at the OCH_2 resonance (dashed purple line) shows a sharp intense resonance of mobile amorphous PEO, which is far from the MOF linkers and therefore does not equilibrate with their magnetization.

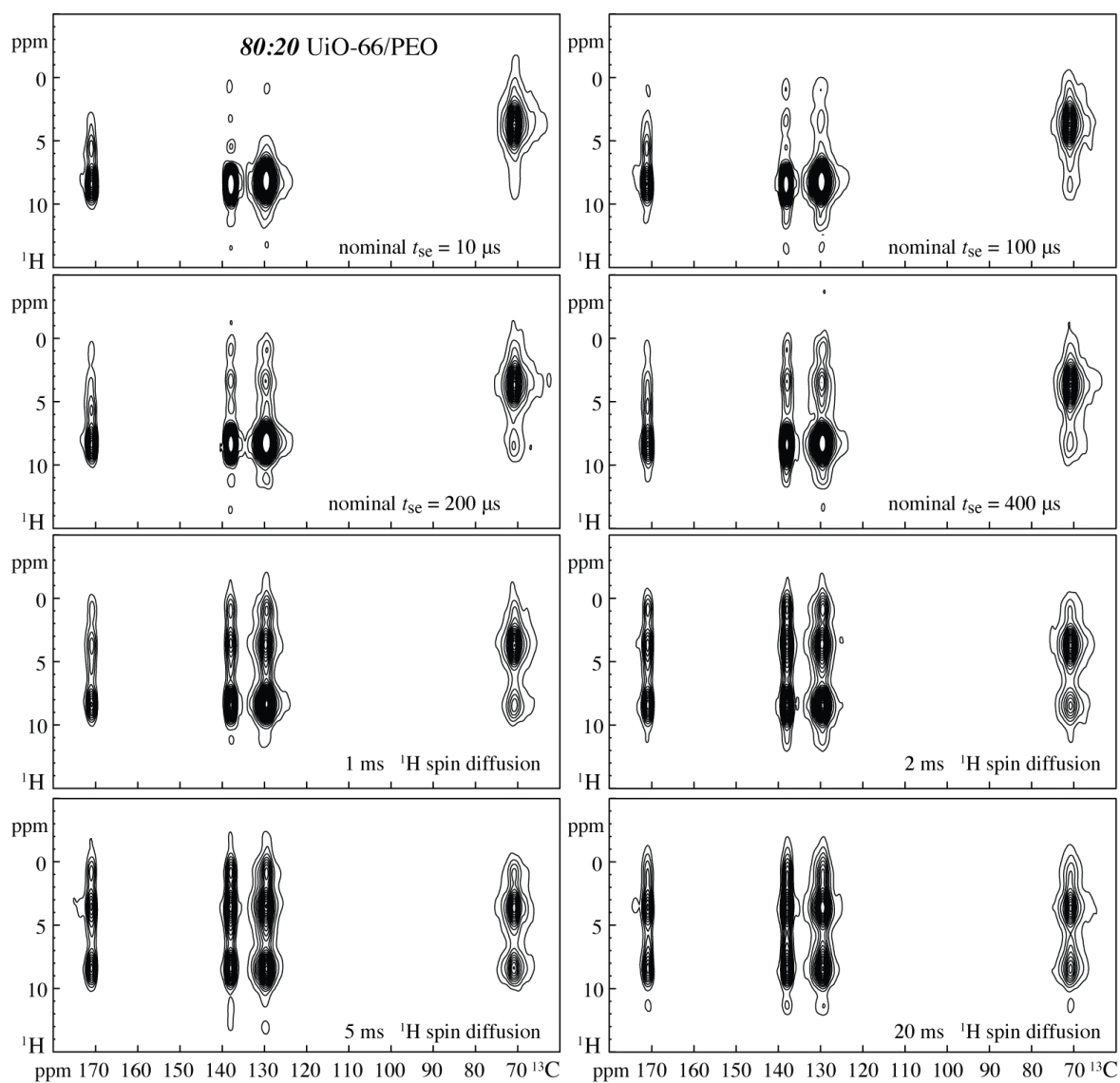


Figure S18. Series of 1H - ^{13}C HetCor spectra of a 80:20 UiO-66/PEO MMM with (nominal) spin-exchange times from 10 μs to 20 ms, as indicated.

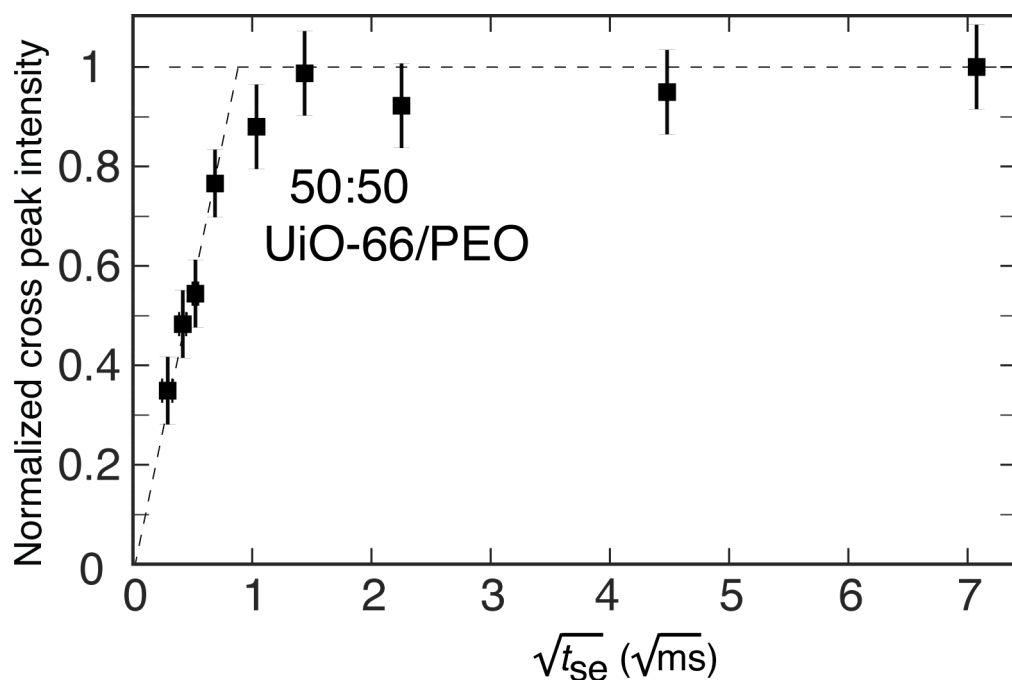


Figure S19. Dependence of the intensity of the cross peak between aromatic H and PEO -CH₂- in ¹H-¹³C HetCor spectra on the square-root of the ¹H spin-exchange time t_{se} in a 50:50 UiO-66/PEO MMM. The linear initial rise is characteristic of spin diffusion.

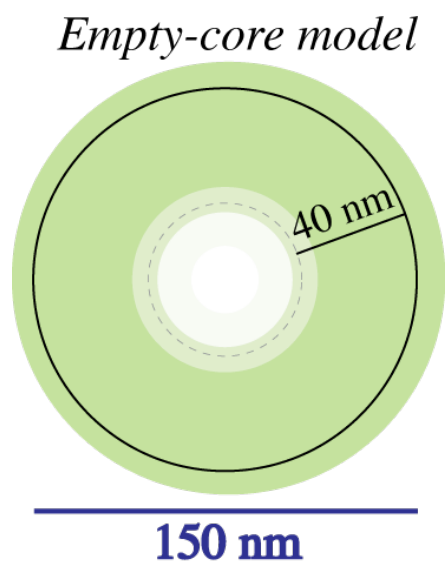


Figure S20. Model with 70-nm diameter PEO-free core in a typical MOF particle, which accounts for 10% of the MOF volume. A larger empty core is excluded by the NMR data.

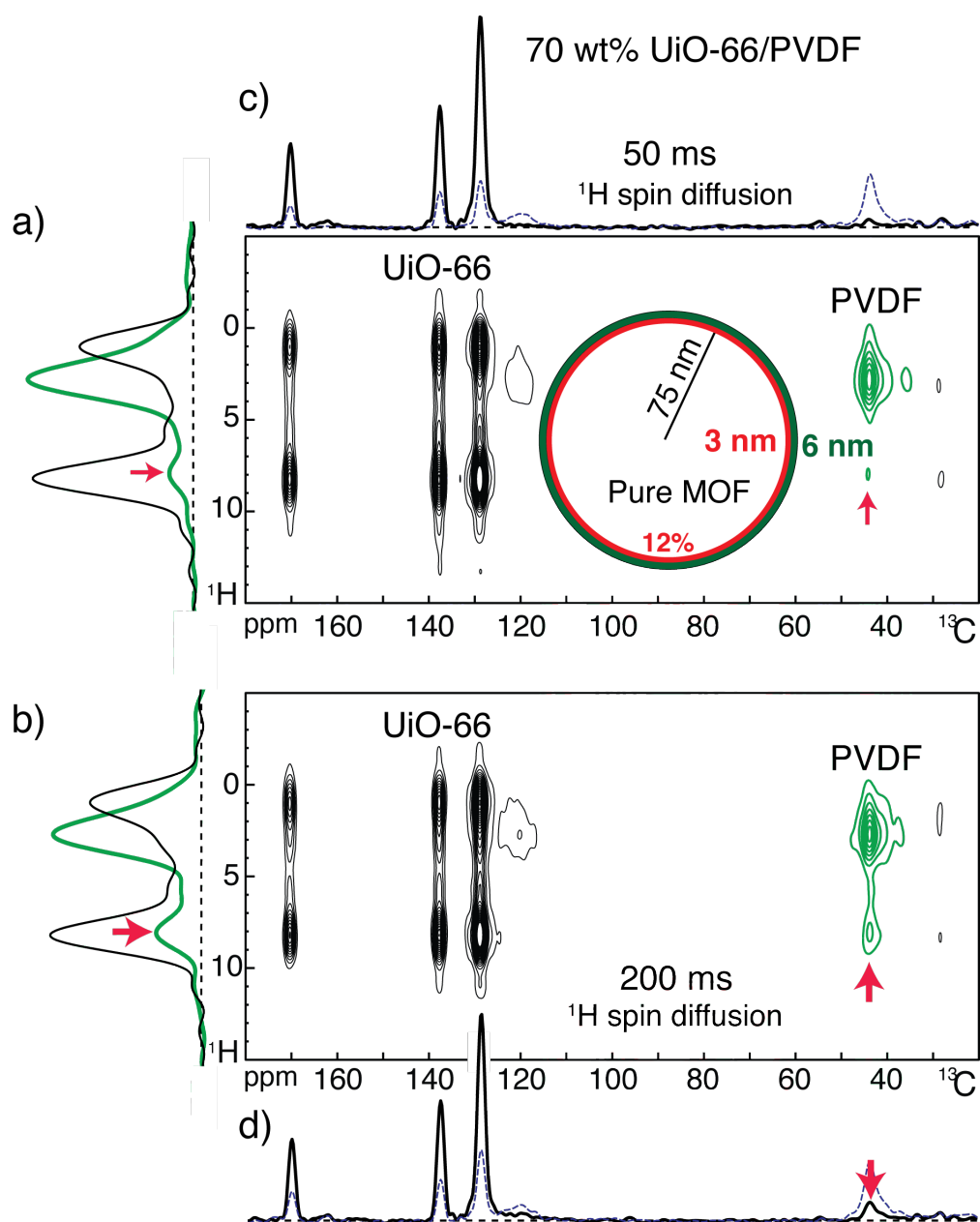


Figure S21. Limited extent of UiO-66–PVDF contacts observed in ^1H - ^{13}C HetCor NMR spectra with ^1H spin exchange. (a) Within 50 ms of spin exchange, little magnetization is transferred from the aromatic protons to PVDF. The inset shows the surface-coating model spin diffusion from the polymer polarizing a MOF layer of 3-nm thickness (in red), corresponding to 12% of the MOF volume. (b) A somewhat stronger cross peak (marked with a red arrow) is observed after a long spin-diffusion time of 200 ms; nevertheless, the vertical cross sections at the UiO-66 and PVDF peak positions shown on the left are still clearly distinct, showing that unlike PEO, PVDF does not homogeneously fill the pores of the MOF.

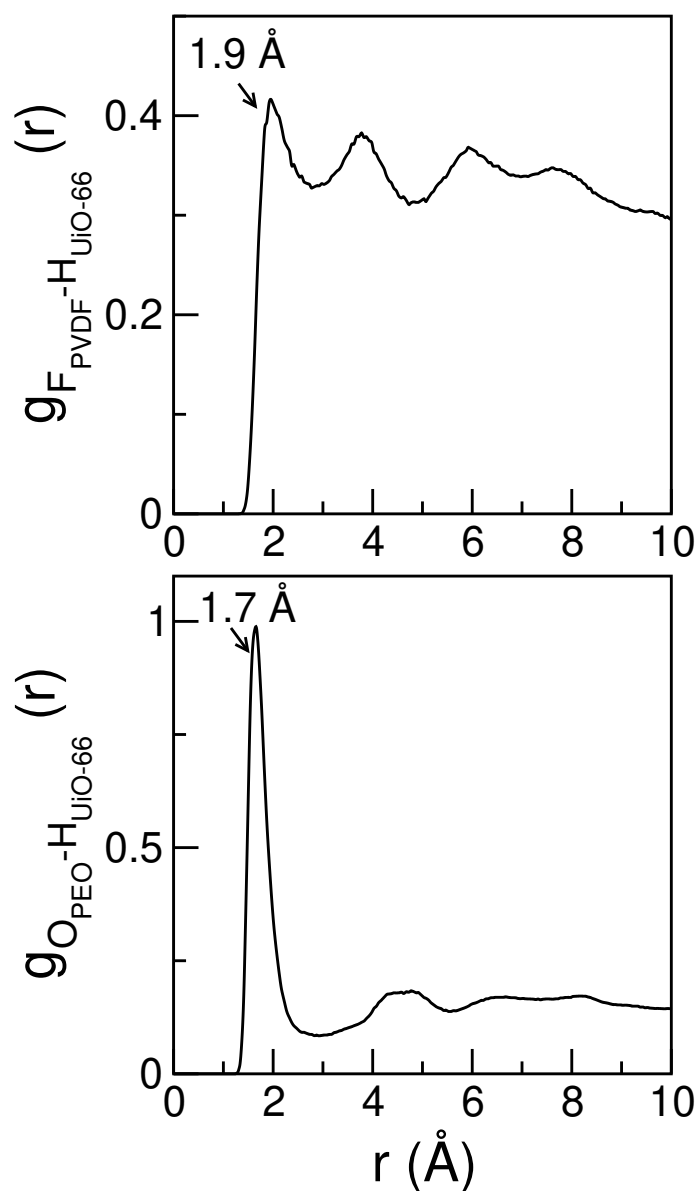


Figure S22. Radial distribution functions (RDFs) for the most relevant interactions between polymer sites and MOF sites at the external part of the surface (OH terminations attached to the surface Zr atoms). Top panel: $F_{PVDF} - H(OH)_{UiO-66}$. Bottom panel: $O_{PEO} - H(OH)_{UiO-66}$. The upper panel of the figure corresponds to the RDFs between the fluorine atoms of PVDF and the hydrogen atoms of the terminal -OH at the UiO-66 surface, while the lower panel represents the RDFs between the oxygen atoms of PEO and the same terminal group. Both RDF pairs show short interacting distances of 1.9 and 1.7 Å, respectively.

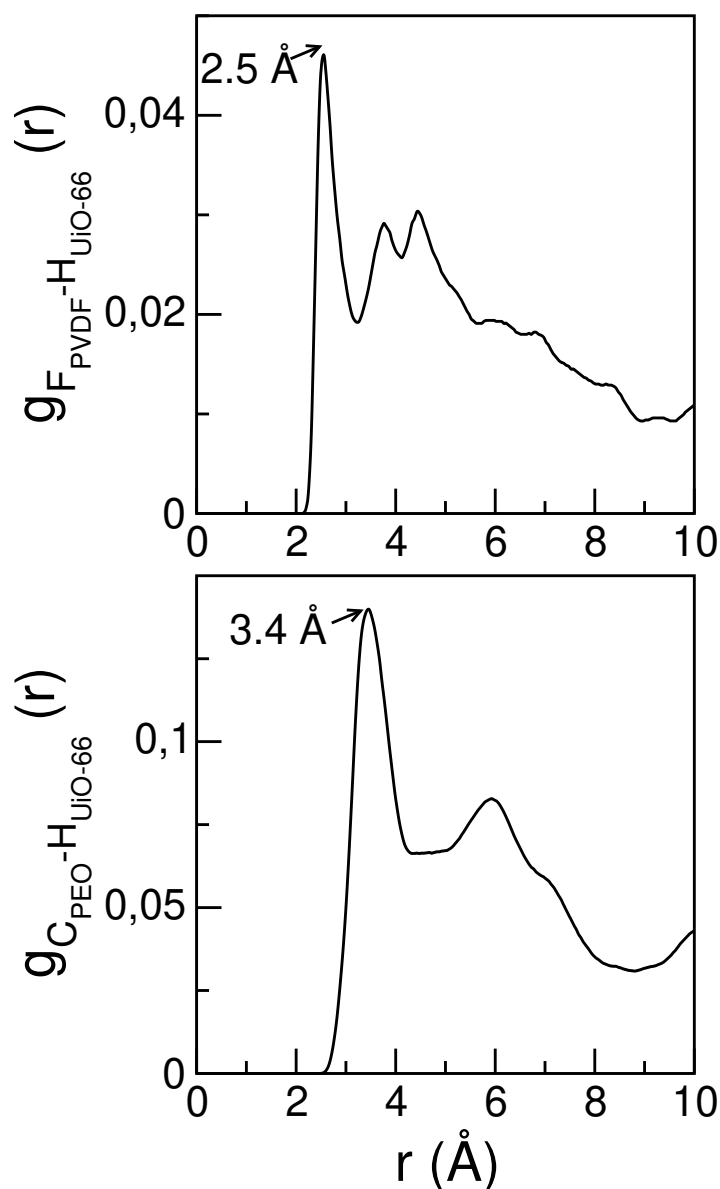


Figure S23. Radial distribution functions for the most relevant interactions between polymer sites and MOF sites at the internal part of the surface (H atoms in the organic linkers). Top panel: $F_{\text{PVDF}} - \text{H}(\text{OH})_{\text{UIO-66}}$. Bottom panel: $C_{\text{PEO}} - \text{H}(\text{OH})_{\text{UIO-66}}$. These plots show that the fluorine atoms of PVDF and the carbon atoms of PEO mostly interact with the organic bdc^{2-} linker, with interacting distances with the H-atoms of the phenyl ring of 2.5 and 3.4 Å, respectively. The difference between the intensities (y-axis) is about a factor of 3 for the interactions with the internal MOF surface groups.

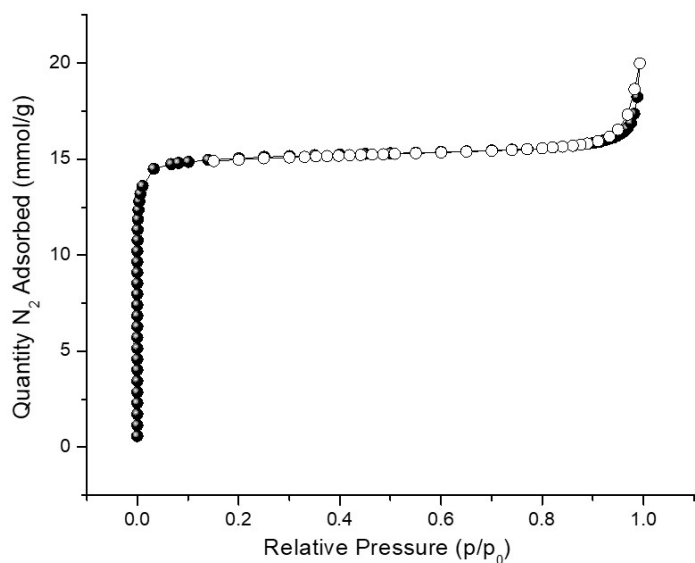


Figure S24. Nitrogen sorption isotherm data of UiO-66 used in this study.

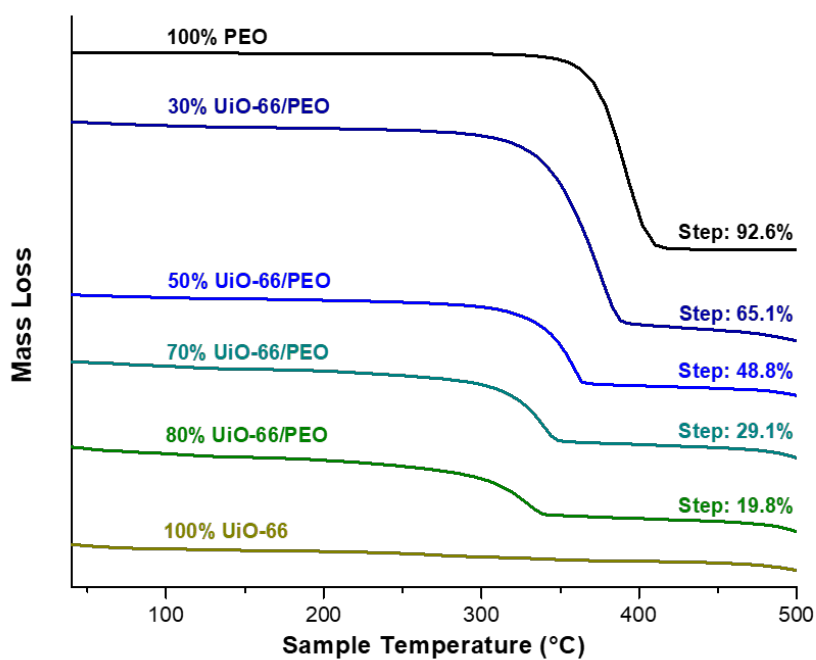


Figure S25. TGA traces of UiO-66/PEO MMMs at different MOF loadings shown above. MMMs show one step feature between 30 and 550°C, which corresponds to degradation of the PEO component, allowing calculation of actual MOF content. Degradation steps shift to lower temperatures as MOF content is increased, corresponding to a significant destabilization of the polymer component as MOF content increases.

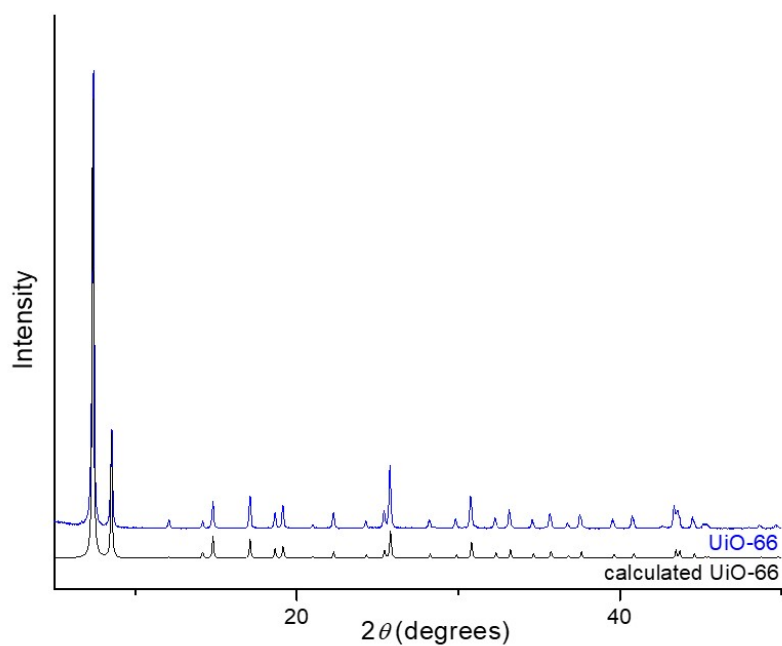


Figure S26. PXR D of as-synthesized UiO-66 used in this study with the calculated powder pattern for comparison.

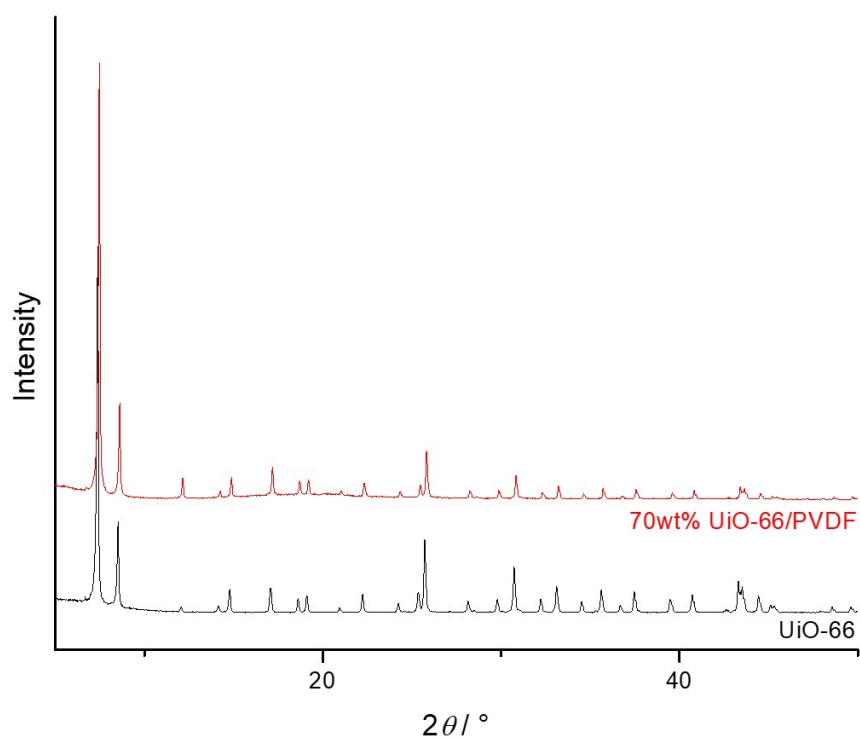


Figure S27. Powder X-ray diffraction patterns of the starting UiO-66 compared to a 70 wt% UiO-66/PVDF MMM demonstrates identical crystallinity, suggesting the MOF retains its crystallinity within this MMM.

REFERENCES

- (1) Abbott, L. J.; Hart, K. E.; Colina, C. M. Polymatic: a generalized simulated polymerization algorithm for amorphous polymers. *Theor. Chem. Acc.* **2013**, *132*, 1334.
- (2) Plimpton, S. Fast parallel algorithms for short-range molecular dynamics. *J. Comput. Phys.* **1995**, *117*, 1-19.
- (3) Semino, R.; Moreton, J. C.; Ramsahye, N. A.; Cohen, S. M.; Maurin, G. Understanding the origins of metal-organic framework/polymer compatibility. *Chem. Sci.* **2018**, *9*, 315-324.
- (4) Perdew, J. P.; Burke, K.; Ernzerhof, M. Generalized gradient approximation made simple. *Phys. Rev. Lett.* **1996**, *77*, 3865-3868.
- (5) Mayo, S. L.; Olafson, B. D.; Goddard, W. A. DREIDING: A generic force field for molecular simulations. *J. Phys. Chem.* **1990**, *94*, 8897-8909.
- (6) Allen, M. P.; Tildesley, D. J. *Computer Simulation of Liquids.* **1987**.
- (7) Hutter, J.; Iannuzzi, M.; Schiffmann, F.; VandeVondele, J. *atomistic simulations of condensed matter systems. Wiley Interdisciplinary Reviews: Computational Molecular Science* **2014**, *4*, 15-25.
- (8) Bravais, A. *Etudes Cristallographiques*; Gauthier-Villars: Paris, 1866.
- (9) Donnay, J. D. H.; Harker, D. A new law of crystal morphology extending the law of Bravais. *Am. Mineral.* **1937**, *22*.
- (10) Friedel, G. Etudes sur la loi de Bravais. *Bull. Soc. Franc. Mineral* **1907**, *30*, 326.
- (11) Johansson, A.; Tegenfeldt, J. NMR study of crystalline and amorphous poly(ethylene oxide). *Macromolecules* **1992**, *25*, 4712-4715.
- (12) Hu, W. G.; Schmidt-Rohr, K. Polymer ultradrawability: the crucial role of α -relaxation chain mobility in the crystallites. *Acta Polym.* **1999**, *50*, 271-285.
- (13) Denny Jr., M. S.; Cohen, S. M. In situ modification of metal-organic frameworks in mixed-matrix membranes. *Angew. Chem. Int. Ed.* **2015**, *54*, 9029-9032.
- (14) Rouquerol, J.; Llewellyn, P.; Rouquerol, F. In *Studies in Surface Science and Catalysis*; Llewellyn, P. L., Rodriguez-Reinoso, F., Rouquerol, J., Seaton, N., Eds.; Elsevier: 2007; Vol. 160, p 49-56.
- (15) Gómez-Gualdrón, D. A.; Moghadam, P. Z.; Hupp, J. T.; Farha, O. K.; Snurr, R. Q. Application of consistency criteria to calculate BET areas of micro- and mesoporous metal-organic frameworks. *J. Am. Chem. Soc.* **2016**, *138*, 215-224.